nature materials

Article

https://doi.org/10.1038/s41563-026-02479-9

A 3-GPa ductile martensitic alloy enabled by interface complexes and dislocations

Received: 4 June 2025

Accepted: 4 January 2026

Rong Lv[1,2,10], Jia Li[3,10], Yunzhu Shi[1,2] ✉, Shuai Dai[1,2], Shuo Wang[3], Xinren Chen[4], Xiaoye Zhou[5], Fei Zhang[6], Meiyuan Jiao[2], Chao Ma[1], Alexander Schökel[7], Shaolou Wei[4], Yan Ma[8], Claudio Pistidda[9], Zhifeng Lei[1,2] ✉ & Zhaoping Lu[2] ✉

Ultrahigh-strength bulk alloys with martensitic structures are essential for heavy-duty applications and infrastructure. However, they often contain small-angle grain boundaries (SAGBs), which enhance ductility but weaken resistance to dislocation motion. This limitation restricts tensile strength to below 2.5 GPa, even when nanoprecipitates or hierarchical architectures are introduced. Here we overcome this limitation by developing a near-single-phase martensitic alloy with a tensile strength exceeding 3 GPa. In the model $(Fe_{49}Co_{40}Mo_{11})_{99.6}B_{0.3}C_{0.1}$ (at.%) alloy, cold rolling followed by low-temperature annealing introduces a high density of dislocations and drives Mo, C and B atoms to cosegregate at the SAGBs, forming interface complexes. These complexes stabilize the SAGBs, reinforce barriers to dislocation motion and still permit dislocation transmission across boundaries. As a result, the alloy achieves a tensile yield strength of 3.05 GPa and a fracture elongation of 5.13%, setting a benchmark for ultrahigh-strength, ductile alloys. This simple, scalable process integrates seamlessly with existing manufacturing methods and opens a path to next-generation structural materials.

Ultrahigh-strength bulk metallic materials underpin advanced structural applications across aerospace, transportation and energy sectors[1–3]. Alloys featuring lath martensite—an outcome of a rapid, diffusionless austenite-to-martensite transformation[4]—have long epitomized the ultrahigh-strength class[5]. Their exceptional strength derives from an ultradense network of dislocations and finely spaced martensitic boundaries, which can elevate the martensitic matrix's yield strength into the 1–1.4 GPa range[6]. In particular, the high fraction (50–70 vol.%) of lath and sub-block boundaries, predominantly small-angle grain boundaries (SAGBs), reinforces the matrix through substantial dislocation strengthening, contributing over 65% of the total strength[7]. Yet, although these SAGBs offer superior coherency with the matrix to facilitate dislocation transmission and accommodate plastic strain[8]—thereby mitigating stress concentration and premature failure—they inherently compromise their ability to impede dislocation motion, thus capping the maximum achievable strength.

---

[1] College of Materials Science and Engineering, Hunan University, Changsha, People's Republic of China. [2] Beijing Advanced Innovation Center for Materials Genome Engineering, State Key Laboratory for Advanced Metals and Materials, University of Science and Technology Beijing, Beijing, People's Republic of China. [3] State Key Laboratory of Advanced Design and Manufacturing Technology for Vehicle, College of Mechanical and Vehicle Engineering, Hunan University, Changsha, People's Republic of China. [4] Department of Microstructure Physics and Alloy Design, Max Planck Institute for Sustainable Materials, Düsseldorf, Germany. [5] Department of Materials Science and Engineering, Shenzhen MSU-BIT University, Shenzhen, People's Republic of China. [6] Institute of High Energy Physics, Chinese Academy of Sciences, Beijing, People's Republic of China. [7] Deutsches Elektronen-Synchrotron DESY, Hamburg, Germany. [8] Department of Materials Science and Engineering, Delft University of Technology, Delft, the Netherlands. [9] Department of Materials Design, Institute of Hydrogen Technology, Helmholtz-Zentrum Hereon GmbH, Geesthacht, Germany. [10] These authors contributed equally: Rong Lv, Jia Li. ✉ e-mail: yzshi@hnu.edu.cn; zflei@hnu.edu.cn; luzp@ustb.edu.cn

Efforts to push martensitic alloys towards higher strength—often through the introduction of high-density precipitates or hierarchical substructures—have met with limited success, typically reaching an upper limit near 2 GPa (refs. 3,9,10). The constraints are multifold: precipitation hardening is restricted by equilibrium solubility, and microstructure-dependent dislocation strengthening suffers from thermodynamic recovery. These intrinsic limitations, combined with the inherent penetrability of SAGBs, have perpetuated a trade-off between strength and ductility, with state-of-the-art alloys rarely surpassing 2.5 GPa in yield strength and often displaying fracture elongations below 3% (refs. 11–13).

Here, we report a 3GPa-class martensitic alloy, $(Fe_{49}Co_{40}Mo_{11})_{99.6}B_{0.3}C_{0.1}$ (at.%), strengthened by dislocations and interface complexes. A streamlined processing route—cold rolling to generate a high density of dislocations and SAGBs, accounting for over 70% of the total boundary fraction, followed by low-temperature annealing—drives the cosegregation of Mo, C and B at these boundaries. This segregation leads to the formation of interface complexes that stabilize the SAGBs and transform them into robust nanoscale barriers to dislocation motion. These stabilized interfaces, together with the dense dislocation network, enhance the yield strength by over 2 GPa while preserving dislocation transmissibility and ductility. The resulting near single-phase martensitic alloy achieves a tensile yield strength of 3.05 GPa coupled with a fracture elongation of 5.13%, thereby redefining the conventional strengthening paradigm and setting a benchmark for ultrahigh-strength structural materials.

Results

Alloy design

To surpass conventional strength limits, we implemented a boundary-segregation engineering strategy designed to maximize dislocation blockage and suppressing crack nucleation[14,15]. Unlike traditional multiphase strengthening, which is inherently limited by the volume fraction and spatial distribution of secondary phases, our approach harnesses high-density dislocations and SAGBs as controllable defect regulators. The alloy-design framework rests on three synergistic pillars: (1) a martensitic matrix, (2) sufficient cold-workability enabling severe plastic deformation to imprint a dense, uniform network of defects, and (3) cosegregation of metallic and interstitial elements to stabilize these defects. Together, the first two guarantee an ample defects reservoir, whereas the third converts that reservoir into a stable, strengthening architecture. Through combinatorial composition optimization and thermomechanical processing design, we developed a Fe–Co–Mo medium-entropy martensitic alloy system, where cobalt thermally stabilizes body-centred cubic martensite[16], while molybdenum induces severe lattice distortion via atomic size mismatch ($\delta = 8.8\%$)[17]. The martensitic matrix naturally harbours a high density of defects (dislocation density $>10^{15}$ m^{-2}), generating synergistic strengthening effects through lattice distortion hardening and solid solution strengthening. The introduction of interstitial atoms, such as boron (0.3 at.%) and carbon (0.1 at.%), enhances hardenability and strengthens interfacial bonding[18–20]. Cold rolling increases dislocation density, and subsequent low-temperature annealing stabilizes these defects through boundary segregation, facilitating the formation of interface complexes that ultimately optimize mechanical performance.

On the basis of the above concept of the alloy design strategy, the composition of the model alloy was established through a thermodynamically guided and experimentally validated process. The Mo content was initially set to 11 at.% based on the ternary phase diagram reported (Supplementary Fig. 1), which ensured the stability of single-phase austenite at high temperature[21]. Subsequent CALculation of PHAse Diagrams (CALPHAD) calculations for the $Fe_xCo_{89-x}Mo_{11}$ system, combined with experimental validation, identified an optimal Fe/Co ratio of 49/40, providing the best balance of strength and ductility after annealing (Supplementary Fig. 2). Systematic variations in Mo content from 5 to 13 at.% identified 11 at.% as optimal for workability and segregation-induced strengthening (Supplementary Figs. 3–6), while effects of B and C on interface complex formation and the resulting mechanical response were verified separately (Supplementary Fig. 7). Ultimately, the final composition was determined as $(Fe_{49}Co_{40}Mo_{11})_{99.6}B_{0.3}C_{0.1}$. The calculated configurational entropy (ΔS_{conf}) of the typical $(Fe_{49}Co_{40}Mo_{11})_{99.6}B_{0.3}C_{0.1}$ alloy is 1.111 R, lying within the range of $0.69\ R \leq \Delta S_{conf} \leq 1.61\ R$ that defines medium-entropy alloys[22]. Full details of the compositional design and optimization procedures are described in the Methods.

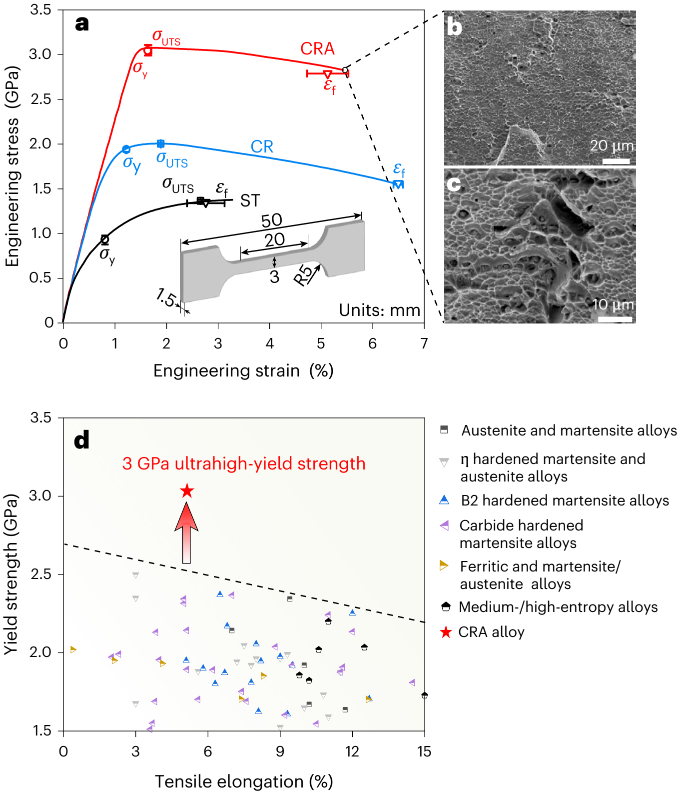

Fig. 1 | Mechanical properties. **a**, Room-temperature tensile engineering stress–strain curves. σ_y represents the yield strength (circles), σ_{UTS} denotes the ultimate tensile strength (squares) and ε_f is the fracture elongation (triangles). ST: the as-cast alloy underwent solution treatment at 1,200 °C for 2 h. CR: the alloy experienced cold rolling with an 85% thickness reduction after ST. CRA: the alloy was annealed at 450 °C for 20 min following CR. The inset shows the tensile sample dimension. The data points and error bars represent the mean ± s.d. taken from four independently tensile samples. **b**, Fracture morphology of the CRA alloy. **c**, Additional fracture morphology details for the CRA alloy. **d**, A comparison of mechanical properties of the CRA alloy with conventional ultrahigh-strength alloys, including austenitic/martensitic alloys[3,10,46–48], ferritic and martensitic/austenite dual-phase alloys[49,50], high-strength martensitic alloys strengthened by second-phase particles[1,2,9,12,13,51–73], and medium-entropy alloys (MEAs)/high-entropy alloys (HEAs)[74–81]. The CRA alloy exhibits an ultrahigh yield strength exceeding 3 GPa.

Mechanical properties

To systematically elucidate the strengthening effect, we conducted comparative investigations on three processing states of the $(Fe_{49}Co_{40}Mo_{11})_{99.6}B_{0.3}C_{0.1}$ medium-entropy alloy: solution-treated (ST, where the as-cast alloy was homogenized at 1,200 °C for 2 h), cold-rolled (CR, where the ST alloy underwent an approximately 85% thickness reduction) and annealed after cold-rolling (CRA, where the CR alloy was annealed at 450 °C for 20 min). Figure 1a shows room temperature tensile engineering stress–strain curves for these alloys. The ST variant demonstrates a tensile yield strength of 0.93 ± 0.05 GPa and a

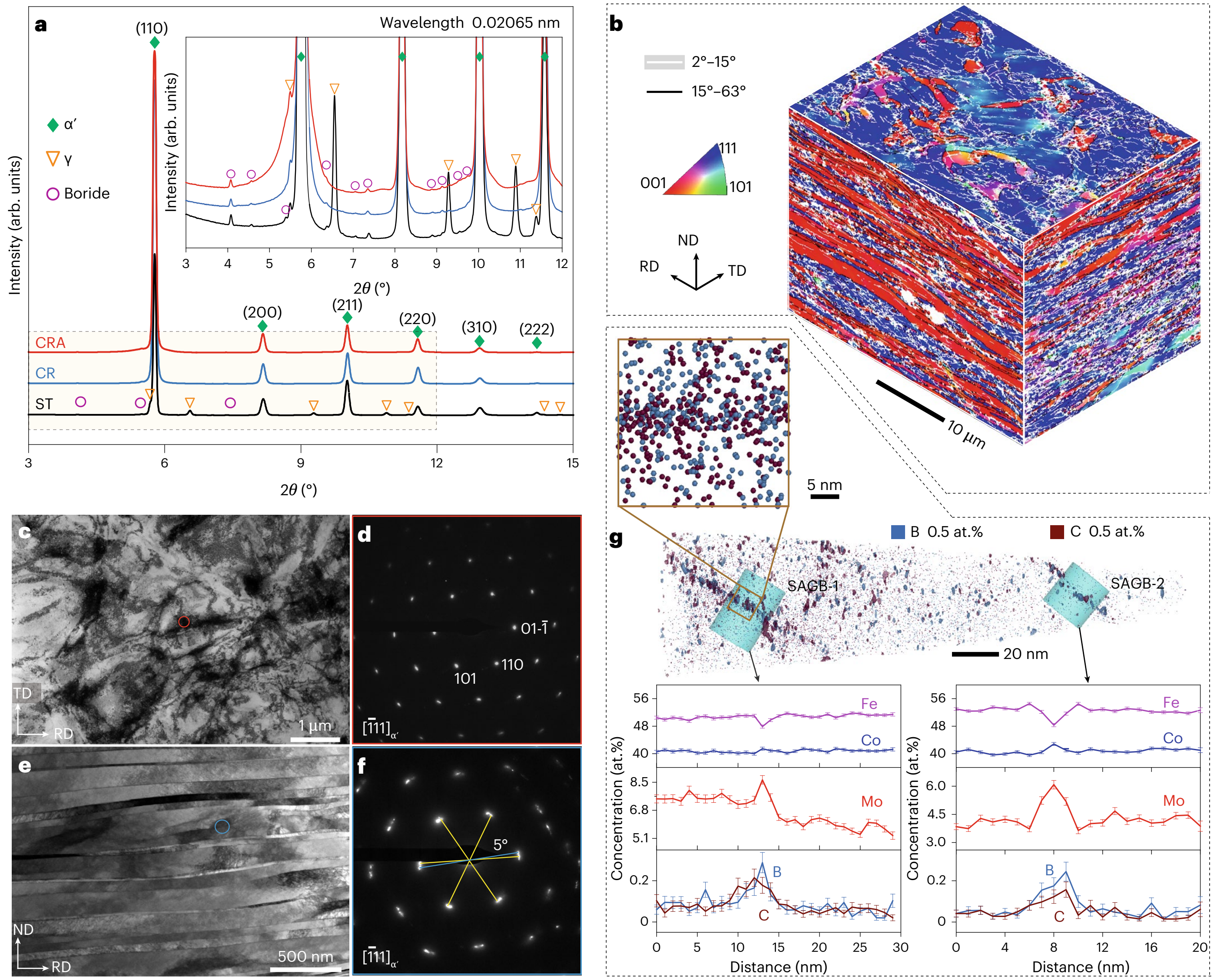

Fig. 2 | Microstructure characterization. **a**, Synchrotron HEXRD patterns of the ST, CR and CRA alloys, along with an enlarged view of the patterns in the inset, showing that the ST alloy consists of martensite, austenite and boride phases, while the CR and CRA alloys are predominantly martensite. **b**, Three-dimensional EBSD image of the CRA alloy, revealing preservation of deformed textures along the <001> and <111> crystallographic directions. The RD, TD and ND are indicated. **c**,**e**, Bright-field TEM images of the CRA alloy, showing massive subgrains within the TD–RD plane (**c**), and a lamellar microstructure within the ND–RD plane (**e**). **d**,**f**, SAED patterns (the selected regions are marked by red and blue circles in **c** (**d**) and **e** (**f**), respectively) of the CRA alloy, highlighting the presence of a single martensitic phase and SAGBs, respectively. **g**, Three-dimensional APT reconstruction of CRA alloy, with iso-composition surfaces of 0.5 at.% for both C and B. The image illustrates the cosegregation of B, C and Mo along SAGBs. The 1D compositional profile (blue cylinders) compares the SAGB and matrix compositions, while the enlarged view (brown square) details the C and B distributions across the SAGB. The error bars are standard deviations of the mean.

fracture elongation of 2.76% ± 0.36%. By contrast, the CR variant features a higher tensile yield strength of 1.94 ± 0.01 GPa, along with an increased fracture elongation of 6.49% ± 0.09%. In particular, the CRA variant exhibits an exceptional tensile yield strength of 3.05 ± 0.01 GPa, which is approximately 2.1 GPa and 1.1 GPa higher than that of the ST and CR variants, respectively. Further repeated tensile curves for the CRA alloy are provided in Supplementary Fig. 8, demonstrating the excellent reproducibility. Moreover, the CRA alloy displays remarkable microhardness, attaining a value of 802 ± 5.9 HV, which surpasses that of the ST (444 ± 3.4 HV) and CR (576 ± 1.6 HV) alloys by 80.6% and 39.4%, respectively (Supplementary Fig. 9). Despite its ultrahigh yield strength, the CRA variant maintains a respectable fracture elongation of 5.13% ± 0.40% (Fig. 1a).

Fracture morphology analysis of the CRA variant reveals numerous dimples (Fig. 1b,c), indicating ductile fracture behaviour. Conversely, the fracture morphology of the ST alloy exhibits large cleavage terraces (Supplementary Fig. 10a–c), suggesting brittle fracture behaviour. The fracture morphology of the CR alloy shows a similar dimpled surface to the CRA variant (Supplementary Fig. 10d–f), revealing ductile fracture behaviour. Figure 1d compares the mechanical properties of the CRA alloy with those of conventional ultrahigh-strength alloys, highlighting that the CRA alloy achieves an ultrahigh yield strength of approximately 3 GPa, exceeding those of previously reported martensitic alloys and medium-/high-entropy alloys.

Microstructures

To uncover the mechanism underlying the ultrahigh strength and the evolution of intrinsic defects in this alloy, we performed a comprehensive microstructural analysis down to the atomic scale. Figure 2a illustrates synchrotron high-energy X-ray diffraction (HEXRD) patterns of the ST, CR and CRA alloys. All three alloys consist of martensite (α′), retained austenite (γ) and a small amount of boride (clearly shown in the inset of Fig. 2a). Using the Rietveld refinement method based on the HEXRD results (Supplementary Fig. 11), we determined the volume fraction of each phase. The ST alloy has a retained austenite volume fraction of 17 vol.%, whereas the CR and CRA alloys have only 2 vol.%. The boride content in all three alloys is less than 0.5 vol.%, which is further confirmed by scanning electron microscopy (SEM) images (Supplementary Fig. 12). Further transmission electron microscopy (TEM) characterization of the ST alloy confirms the presence of nanoscale γ and M_4B-type borides with a hexagonal close-packed (hcp) crystal structure, as verified by selected-area electron diffraction (SAED) and energy-dispersive spectrum (EDS) mapping (Supplementary Fig. 13a–g). Both γ and boride phases retain their morphology and distribution after tensile fracture (Supplementary Fig. 13h–j). Figure 2b presents the inverse pole figures of the CRA alloy along the rolling direction (RD), normal direction (ND) and transverse direction (TD). The CRA alloy exhibits a distinct deformation texture, characterized by strong <001> and <111> orientations. Moreover, the matrix is enriched with a substantial fraction of SAGBs, accounting for approximately 71% of the total grain boundary population (Supplementary Fig. 14). Figure 2c,e shows the bright-field TEM images for the TD–RD plane and ND–RD plane in the CRA alloy. The matrix reveals a laminated grain structure, with individual layers measuring tens of nanometres in thickness. Figure 2d presents the SAED pattern corresponding to the region indicated by the solid red circle in Fig. 2c, demonstrating the presence of a single α′ martensitic phase and the absence of nanoprecipitates. Figure 2f depicts the SAED pattern for the area indicated by the solid blue circle in Fig. 2e, illustrating a SAGB with a tilt angle of 5°. Further atom probe tomography (APT) measurements of the CRA alloy reveal the distribution of atoms in the martensite matrix along two random SAGBs with pronounced carbon and boron segregation (Supplementary Fig. 15). Isosurface reconstructions at 0.5 at.% C and 0.5 at.% B concentrations (Fig. 2g) delineate two distinct SAGBs, designated SAGB-1 and SAGB-2. High-resolution atom maps confirm notable segregation of boron and carbon along these boundaries. The concentrations of boron (B) and carbon (C) at the SAGBs are approximately 0.2 at.%, roughly twice the levels found in the grain interior (~0.1 at.%). Molybdenum also segregates at the SAGBs, with concentrations of 8 at.% and 6 at.% at SAGB-1 and SAGB-2, respectively—65% and 22% higher than in the surrounding grain interior. The CR alloy also exhibits strong <001> and <111> textures, with a high volume fraction of SAGBs (~80%) (Supplementary Fig. 16). This alloy also contains a nearly single α′ martensitic phase with a high density of dislocations (4.08×10^{15} m^{-2}) and lamellar grains (Supplementary Fig. 17). However, the element distribution in the CR alloy is uniform, with no notable elemental segregation (Extended Data Fig. 1). These observations suggest that both the CRA and CR alloys are predominantly composed of a martensitic phase enriched with SAGBs. Nevertheless, in the CRA alloy, pronounced cosegregation of Mo, B and C is observed at the SAGBs, leading to the formation of interface complexes.

Deformation behaviour

To decipher the impact of interface complexes on microstructural evolution during deformation, we examined the deformation substructures of the $(Fe_{49}Co_{40}Mo_{11})_{99.6}B_{0.3}C_{0.1}$ CRA and CR alloys both before and after tensile testing. Bright-field TEM images of the CRA and CR alloys before testing (Fig. 3a,b) reveal dense, tangled dislocation networks between lath structures in both materials. However, the lath boundaries in the CRA alloy are distinctly sharp, with widths below 3 nm (Fig. 3a, yellow arrows), whereas those in the CR alloy are more diffuse, exceeding 6 nm in width (Fig. 3b, green arrows). This difference suggests that dislocation recovery near the lath boundaries occurred in the CRA alloy during annealing at 450 °C for 20 min, leading to sharper boundary features. This effect is probably due to grain boundary relaxation and a concomitant reduction in dislocations stored close to grain boundaries[15]. After tensile deformation to fracture, the sharp lath boundaries observed in the CRA alloy became blurred (Fig. 3c), whereas the diffuse boundaries in the CR alloy remained unchanged (Fig. 3d). In the CRA alloy, deformation activated numerous dislocation sources, leading to the accumulation of dislocations near the lath boundaries and generating strain fields or distortions that blurred the boundaries.

In situ HEXRD measurements were performed to quantitatively analyse the microstructure evolution of the alloys during deformation. The diffraction profiles of the CRA alloy under tensile loading are shown in Fig. 3e, revealing no evidence of phase transformation throughout the deformation process. This result confirms that deformation occurred entirely within the existing microstructure, meaning that the martensitic microstructure was responsible for accommodating the plastic deformation. The gradual broadening of diffraction peaks with increasing strain indicates a rise in defect density, which is attributed to the accumulation of dislocations (ranging from 5.66×10^{15} m^{-2} at 0.5% strain to 2.48×10^{16} m^{-2} at 2% strain). Similar in situ HEXRD data for the CR alloy, shown in Supplementary Fig. 18, also reveal no phase transformation, with peak broadening corresponding to an increase in defect density (from 6.95×10^{15} m^{-2} at 0.5% strain to 1.64×10^{16} m^{-2} at 2% strain) during deformation. Using a modified Williamson–Hall analysis of the in situ HEXRD data (detailed in Supplementary Note 1), we determined the evolution of dislocation density in both alloys, as shown in Fig. 3f. Initially, the CRA alloy exhibits a dislocation density 18.6% lower than that of the CR alloy. However, as deformation progresses, the dislocation density in the CRA alloy increases sharply, reaching 1.5 times higher than that of the CR alloy at later stages of deformation. This finding indicates a superior dislocation storage capacity in the CRA alloy, which is closely related to its ductility under super-high flow stress.

Discussion

Formation of interface complexes

Annealing the CR $(Fe_{49}Co_{40}Mo_{11})_{99.6}B_{0.3}C_{0.1}$ (at.%) martensitic alloy at 450 °C for 20 min promotes the cosegregation of Mo, C and B at SAGBs, leading to the formation of interface complexes. We define interface complexes as defect-mediated cosegregation structures in which metallic and interstitial solutes collectively segregate along high-density SAGBs without forming clusters or ordered phases. This configuration substantially enhances interfacial cohesion and preserving the intrinsic body-centred cubic boundary structure, as confirmed by HEXRD, SAED (Fig. 2) and atomic-scale scanning transmission electron microscopy in high-angle annular dark field mode, Kikuchi diffraction and EDS analyses (Supplementary Fig. 19) that revealed no secondary phases. Unlike classical grain boundary complexions—which describe equilibrium thermodynamic states characterized by discrete boundary transitions—our interface complexes represent continuous, kinetically regulated segregation layers. Their high boundary density and tailored chemistry enable a synergy between strength and ductility. These solute-decorated SAGBs are pivotal to the observed tensile strength above 3 GPa and offer a avenue for designing next-generation structural alloys via interface engineering. Understanding the mechanisms driving this cosegregation is key to controlling interface chemistry and structure. According to Gibbs adsorption theory, elemental segregation is primarily driven by the reduction of interfacial free energy[23]. In this alloy, the high density of dislocations and SAGBs in the martensitic matrix provides both structural pathways and energetic favourability for the formation of complexes. Supersaturated solute concentrations further amplify the segregation driving force through enhanced lattice distortion and chemical potential. Cold rolling strengthens these effects by increasing dislocation density and associated distortion energy. During annealing at approximately 0.3 T_m (ref. 24) (where T_m is the melting temperature), thermal activation enables solute diffusion. Dislocations serve as fast diffusion channels[25,26], whereas a high

https://doi.org/10.1038/s41563-026-02479-9

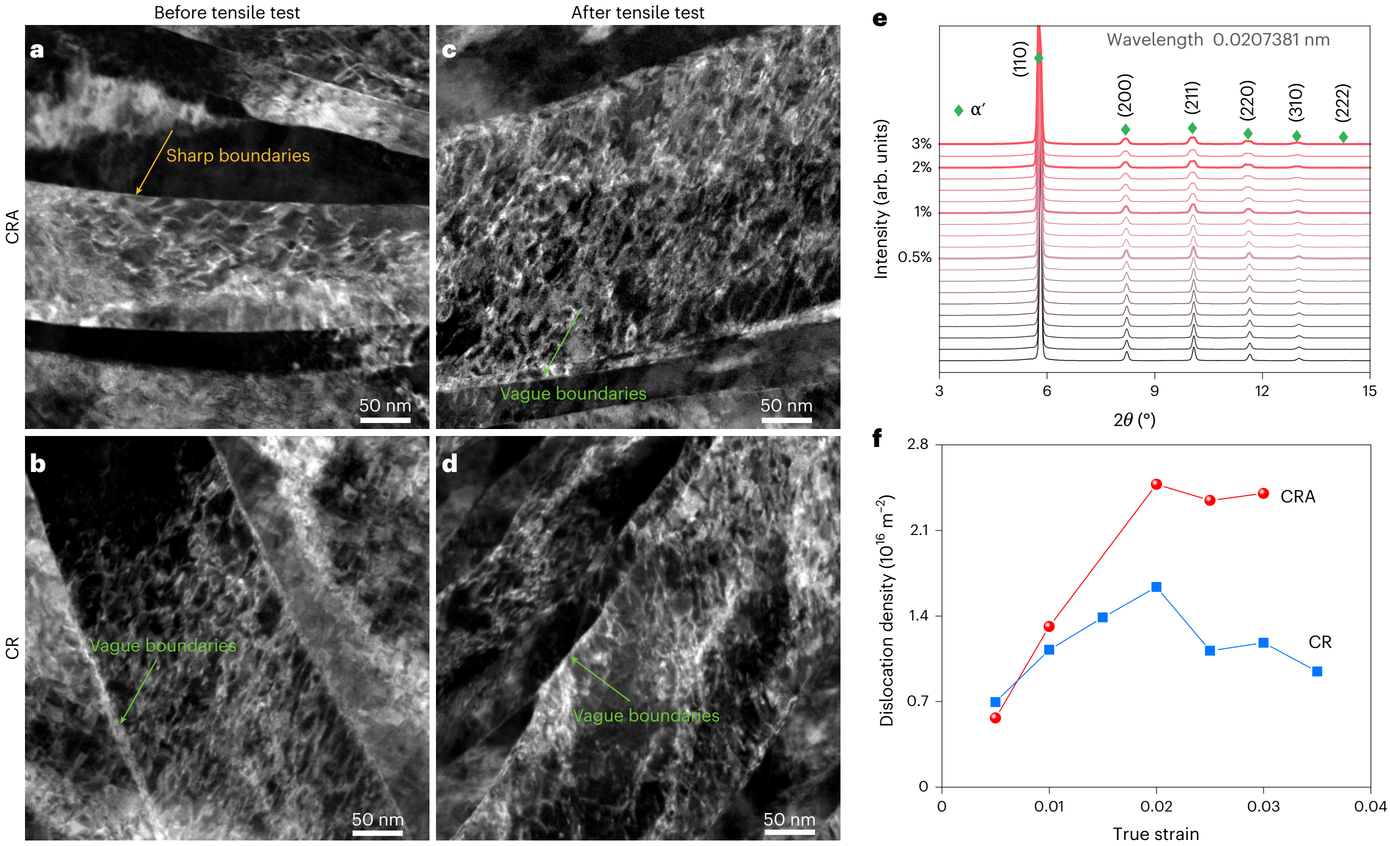

Fig. 3 | Microstructure evolution of CRA and CR alloys during tensile deformation. a,**b**, Bright-field TEM images of the CRA (**a**) and CR (**b**) alloys before tensile testing, showing a high density of dislocations and fine subgrains within martensite laths. The CRA alloy exhibits distinct, sharp lath boundaries, whereas the CR alloy exhibits diffuse lath boundaries. **c**,**d**, Post-tensile microstructures of the CRA (**c**) and CR (**d**) alloys, illustrating the evolution of lath boundaries. In the CRA alloy, initially sharp lath boundaries became vague following deformation, whereas the diffuse lath boundaries of the CR alloy remain unchanged. **e**, In situ HEXRD profiles of the CRA alloy along the loading direction at different tensile true strains, showing no phase transformation and progressive peak broadening with strain, indicative of increasing defect density. **f**, Dislocation density evolution in CRA and CR alloys as a function of true strain. The dislocation density of the CRA alloy increases rapidly during early deformation, surpassing that of the CR alloy in the late plastic deformation stage, reflecting enhanced dislocation storage capability in the CRA alloy.

vacancy density promotes non-equilibrium segregation[27,28], collectively accelerating solute migration to internal interfaces and facilitating the rapid assembly of interface complexes.

Furthermore, configurational entropy (ΔS_{conf}) plays a pivotal role in enabling high supersaturation of solute atoms, thereby providing both kinetic and chemical driving forces for the formation of interface complexes. By analysing the relationship between configurational entropy (ΔS_{conf}) and the strengthening contribution from interface complexes ($\Delta\sigma_{\mathrm{interface\ complexes}}$) across all alloy systems investigated (Supplementary Table 1), we found that, within a single matrix family, for example, the $(\mathrm{Fe}_{60-x}\mathrm{Co}_{40}\mathrm{Mo}_x)_{99.6}\mathrm{B}_{0.3}\mathrm{C}_{0.1}$ ($x = 5, 7, 9, 11$ and 13 at.%) series, a positive correlation between ΔS_{conf} and $\Delta\sigma_{\mathrm{interface\ complexes}}$ exists, indicating that configurational entropy facilitates formation of interface complexes. Across chemically distinct systems, such as between $(\mathrm{Fe}_{50}\mathrm{Co}_{40}(\mathrm{TiVMoW})_{10})_{99.6}\mathrm{B}_{0.3}\mathrm{C}_{0.1}$ and $(\mathrm{Fe}_{60}\mathrm{Co}_{20}\mathrm{Ni}_{15}\mathrm{Mo}_5)_{99.6}\mathrm{B}_{0.3}\mathrm{C}_{0.1}$ alloys, however, no universal correlation exists; matrix-specific chemistry and kinetics dominate.

In fact, ΔS_{conf} does not directly induce interface complex formation but promotes it indirectly by stabilizing supersaturated solid solutions. Higher configurational entropy suppresses precipitation of brittle intermetallic compounds and enhances solute solubility, thereby increasing lattice distortion and defect density during cold rolling. On annealing, these defects provide fast diffusion pathways, whereas the supersaturated solutes contribute both chemical potential and mobility for redistribution. Consequently, elevated ΔS_{conf} ultimately provides the kinetic pathway for interface complex formation by enhancing solute solubility and preventing formation of brittle phases, collectively ensuring both strengthening and good processability of the alloy.

In addition to the driving forces, the intrinsic characteristics of the elements also influence the formation of interface complexes. Using the Arrhenius equation[29,30], we calculated the diffusion coefficients D for all constituents. The diffusion coefficient for B and C is 9–10 orders of magnitude higher than that for Fe, whereas the diffusion coefficient for Mo is 3 orders higher than that for Fe (Supplementary Table 2). The diffusion distances L for C, B and Mo, estimated using $L \approx (Dt)^{1/2}$ with diffusion time $t = 1{,}200$ s, are 4.52 μm, 2.73 μm and 21 nm, respectively (D denotes the diffusion coefficient of each element). The larger diffusion distances for B and C compared with the scale of the lamellar nanostructure in the deformed CR alloy indicate that B and C can be redistributed extensively during annealing. In addition, the more negative mixing enthalpies between Mo and B/C compared with those between Mo and Fe/Co (Supplementary Table 3) suggest a strong chemical affinity between Mo and B/C during annealing[31]. This drives the cosegregation of Mo with B and C along SAGBs, resulting in the formation of interface complexes.

To delve deeper into the energy dynamics of the formation of interface complexes, we used a hybrid density functional theory/Monte Carlo (MC) method to calculate the energy changes caused by Mo segregation at small-angle tilt grain boundaries (Supplementary Note 2). The atomic structures of the $[001](5\bar{1}0)$ and $[00\bar{1}](5\bar{1}0)$ boundaries

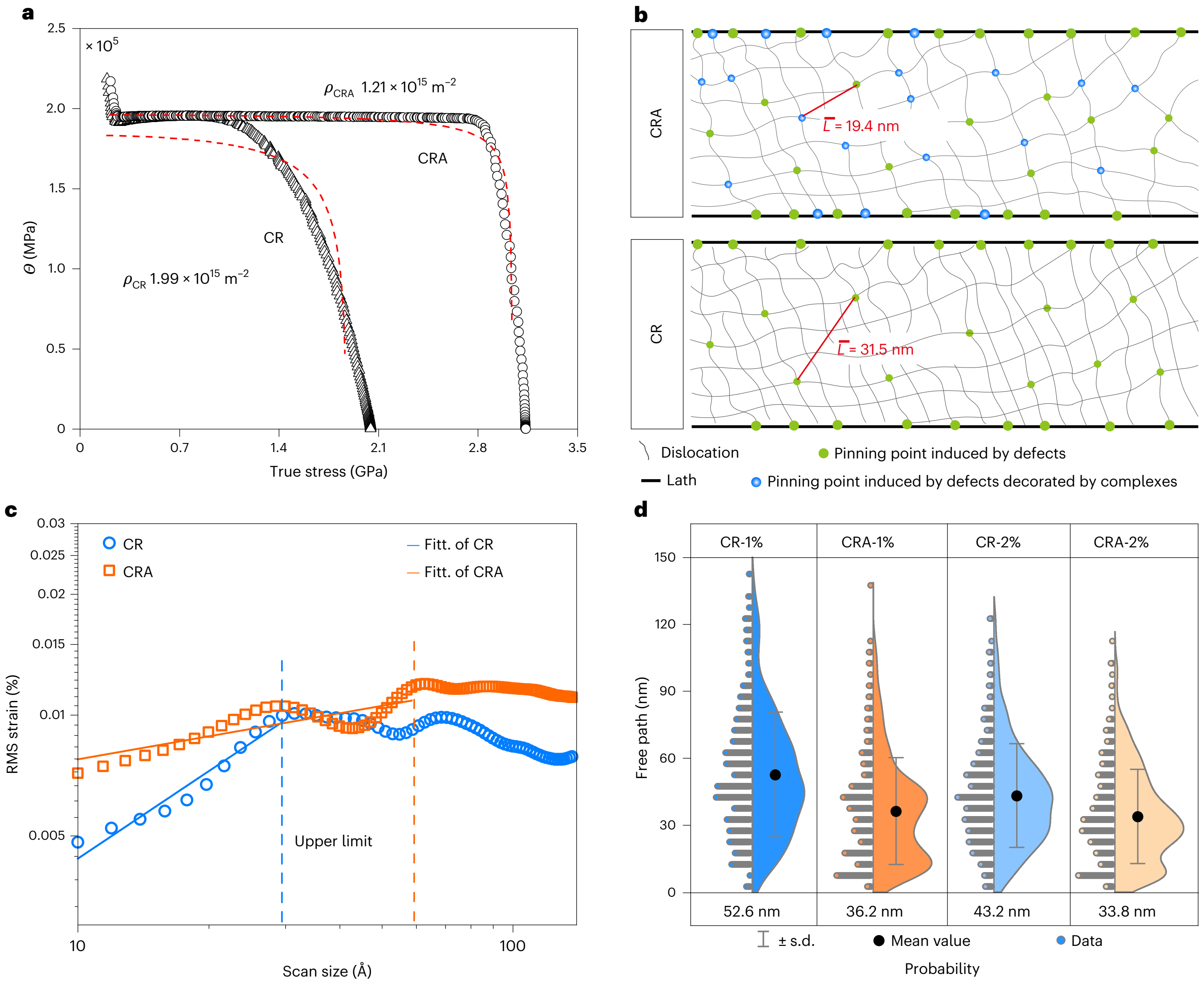

Fig. 4 | Quantification of dislocation structure parameters for the CRA and CR alloys. a, Extended Kocks–Mecking plot for the CRA (circles) and CR (triangles) alloys. The dashed red lines represent the model fitting based on equation (1). Θ denotes the work-hardening rate, and ρ_{CR} and ρ_{CRA} represent the dislocation densities in the CR and CRA alloys, respectively. **b**, Microstructural schematic of the CRA and CR alloys during the pre-yield stage. $\bar{L}$ represents the dislocation segment lengths. The CRA alloy exhibits a lower dislocation density and shorter dislocation segment lengths compared with the CR alloy. **c**, Root mean square (RMS) of the residual strain as a function of scan size, shown in a log–log plot. Fitt., the linear fit of the RMS-scan size curve. **d**, Mean free path of dislocations in the CRA and CR alloys at 1% and 2% residual strain, calculated using the discrete dislocation dynamics method. Data points and error bars denote the mean distance ± s.d. measured from 99 dislocation nodes to their nearest dislocation segments on the slip plane.

before and after 500 MC swaps are shown in Supplementary Fig. 20a,b. After 500 MC swaps, noticeable Mo segregation near these boundaries was observed. The energy evolution of the system over MC steps reveals a sharp decrease in the initial 100 steps, followed by a gradual decline (Supplementary Fig. 20c). This rapid initial energy reduction suggests that even minor Mo segregation substantially stabilizes SAGBs through boundary relaxation and a reduction in boundary excess energy. The results confirm the energetic favourability of Mo segregation, coupled with the more negative mixing enthalpies between Mo and B/C, which drives their cosegregation at SAGBs and leads to the formation of interface complexes (Fig. 2g). After Mo segregation, the grain boundary energy decreased by 0.07 eV Å^{-2}, whereas the grain boundary fracture energy increased by 0.049 eV Å^{-2} (Supplementary Fig. 20d), highlighting the substantial impact of segregation on grain boundary properties. Given that both CRA and CR alloys exhibit dimple fracture morphology, indicative of transgranular fracture (Fig. 1b,c and Supplementary Figs. 10e,f), the reduction in grain boundary energy enhances boundary stability—particularly beneficial for the yield strength of nanostructured materials. Simultaneously, the increase in grain boundary fracture energy reflects improved boundary cohesion, conferring enhanced fracture resistance and contributing to improved ductility.

Role of interface complexes

To assess the impact of the interface complexes on strengthening, we quantitatively analysed dislocation segment lengths in CRA and CR alloys using the extended Kocks–Mecking model[32,33]. In crystalline metals, the initial microstructure comprises dislocation lines and lattice defects. Dislocations interact through their surrounding strain fields, forming a continuous network, known as the Frank net[34]. This network interacts with microstructural features such as solute atoms, grain boundaries, other dislocations and precipitates. The points at which these interactions occur, referred to as pinning points, impede dislocation motion. Dislocation density and the distribution of dislocation segment lengths—the distance between these pinning points—are key factors influencing the strength and deformation behaviour. Van et al.[33] demonstrated that the extended Kocks–Mecking model enables the estimation of these parameters before plastic deformation, based on tensile curves. The corresponding equations and computational procedures are provided in Supplementary Note 3.

The extended Kocks–Mecking plots for CRA and CR alloys in the pre-yield stage were fitted. The results, shown by the dashed red lines in Fig. 4a, closely align with the experimental data from the Kocks–Mecking model. The fitting parameters—the dislocation density ρ and the dislocation segment lengths $\bar{L}$—are 1.21×10^{15} m^{-2} and 19.4 ± 0.01 nm for the CRA alloy, and 1.99×10^{15} m^{-2} and 31.5 ± 0.04 nm for the CR alloy, respectively. The dislocation densities of the two alloys are comparable and align with values obtained from HEXRD measurements, confirming the validity of this model. These results suggest that interface complexes in the CRA alloy mechanically stabilize SAGBs, increasing the number of effective pinning points and reducing dislocation segment lengths $\bar{L}$. Specifically, the CRA alloy exhibits a 38% shorter average dislocation segment lengths $\bar{L}$ compared with the CR alloy (Fig. 4b). This indicates that interface complexes transform unstable SAGBs (that is, unstable pinning points) into more stable ones (that is, stabilized SAGBs; Fig. 4b, blue dots), effectively hindering dislocation motion at higher stresses and markedly enhancing the yield strength of the CRA alloy.

To further elucidate the role of interface complexes in strengthening, we quantified the yield strength contributions in both the CRA and CR alloys. The detailed calculation process is provided in Supplementary Note 4. A comparison between the calculated and experimental yield strengths for both alloys is shown in Extended Data Fig. 2. For the CRA alloy, the calculated yield strength agrees well with experimental results, with solid-solution hardening and dislocation strengthening identified as the primary contributors. However, for the CRA alloy, there is an evident discrepancy of approximately 1.4 GPa between the calculated ($\Delta\sigma_{\mathrm{Cal.1}}$) and experimental yield strengths when using the same grain boundary strengthening as in the CR alloy. This discrepancy probably arises from the presence of interface complexes, which stabilize SAGBs and alter their interaction with dislocations, thereby providing an additional strengthening contribution.

To clarify this point, we calculated the residual strain field distribution near the SAGBs in both alloys using the discrete dislocation dynamics method (Supplementary Note 5). The CRA alloy exhibits a larger upper limit and longer wavelength for the strain field induced by deviatoric lattice distortion compared with the CR alloy (Fig. 4c and Supplementary Fig. 21). This indicates that interface complexes generate a stronger strain field, which conducively impedes dislocation motion across these boundaries[35,36]. Consequently, the dislocation mean free path in the CRA alloy is shorter than that in the CR alloy (Fig. 4d), indicating a higher density of dislocation barriers during tensile deformation[37]. This increased barrier density enhances dislocation interactions and facilitates efficient dislocation storage, thereby promoting strain hardening and contributing to improved ductility. The mean free path was determined by statistically measuring the distances between dislocations and calculating the average, with snapshots of the dislocation structures provided in Supplementary Fig. 22. The interface complexes in the CRA alloy strengthen the strain field at SAGBs, increasing resistance to dislocation motion and reducing the dislocation mean free path. This, in turn, contributes to the higher strength of the CRA alloy. To quantify this effect, we substituted the grain size of the lamellar SAGBs in the CRA alloy into the Hall–Petch equation for strengthening. The calculated yield strength ($\Delta\sigma_{\mathrm{Cal.2}}$) closely matches the experimental value (Extended Data Fig. 2), suggesting that interface complexes considerably enhance grain boundary strengthening by making the SAGBs behave similarly to high-angle grain boundaries in terms of their contribution to yield strength in the CRA alloy.

To explore the origin of the ductility of the CRA alloy, we performed stress relaxation experiments. The stress relaxation curves at a true strain of 0.018 for the CRA and CR alloys are shown in Supplementary Fig. 1a,b. We then measured the apparent activation volume ($V^{\mathrm{app.}}$) for both CRA and CR alloys at this strain (Supplementary Fig. 23c, with the calculation process detailed in the Methods). $V^{\mathrm{app.}}$ represents the volume of material involved in a thermally activated process under external loading[38–40] and is directly linked to the interaction between mobile dislocations and short-range obstacles in their slip planes[38]. The $V^{\mathrm{app.}}$ values for both alloys are similar. However, the CRA alloy requires a higher external stress (3 GPa) to surmount internal pinning sites and activate the same $V^{\mathrm{app.}}$. Given their similar microstructures, it is likely that the Frank–Read sources in both alloys have comparable characteristics. Despite this, the CRA alloy needs higher stress to activate these sources. The enhanced stability of SAGBs through interface complexes formation not only increases the critical stress required for plastic deformation, contributing to the alloy's ultrahigh yield strength, but also enhances dislocation storage capacity. This storage is facilitated by dislocation pile-ups at high-angle grain boundaries and an increased number of Frank–Read dislocation sources enabled by the stabilized SAGBs. These factors collectively account for the higher dislocation density and reduced mean dislocation free path observed in the CRA alloy during plastic deformation. Nevertheless, the CRA alloy exhibited slightly lower tensile elongation than the CR alloy. We attribute this apparent discrepancy between higher dislocation density (Fig. 3f) and reduced total ductility (Fig. 1a) to the competition between enhanced dislocation storage and diminished damage tolerance. Efficient dislocation accumulation sustains strain hardening (Supplementary Fig. 24) and elevates the flow stress beyond 3 GPa, but the resulting extreme stress state accelerates void nucleation and crack initiation. Thus, although dislocation mediated hardening extends uniform deformation, final fracture occurs earlier, limiting overall elongation. The similar $V^{\mathrm{app.}}$ values suggest that the stabilized SAGBs in the CRA alloy are as traversable as those in the CR alloy, enabling effective dissipation of high flow stresses and preventing excessive local stresses. Furthermore, the cosegregation of Mo and B enhances boundary cohesion[27,41–45]. As a result, the high density of stable SAGBs strengthens the CRA alloy while maintaining a reasonable degree of ductility at super-high flow stresses.

Conventional martensitic lath boundaries form rapidly during phase transformation. As dense, high-energy defect structures, they strengthen the material but block dislocation transmission, leading to early crack initiation and limiting ductility. By contrast, the SAGBs engineered in this study were produced by cold rolling and annealing, which reorganize dislocations into ordered, low-energy configurations described by the Read–Shockley model[35]. The resulting dense, uniform network of SAGBs accelerates solute diffusion during annealing, promoting widespread formation of Mo–B–C interface complexes that stabilize the boundaries. Consequently, strengthening shifts from dislocation tangles in the CR state to Hall–Petch blocking in the CRA state. These decorated SAGBs effectively impede slip yet remain semi-permeable to dislocations, delaying stress concentration and crack initiation—delivering the exceptional 3.05 GPa yield strength with 5.13% tensile elongation. Thus, the interface complex-decorated SAGBs are central to the strength–ductility synergy of the alloy.

To further substantiate the critical role of interface complexes, we conducted low-temperature annealing of the cold-rolled $(\mathrm{Fe}_{60-x}\mathrm{Co}_{40}\mathrm{Mo}_x)_{99.6}\mathrm{B}_{0.3}\mathrm{C}_{0.1}$ ($x = 7$, 9 and 11 at.%) alloys with varying Mo contents, as well as on a $\mathrm{Fe}_{49}\mathrm{Co}_{40}\mathrm{Mo}_{11}$ alloy without C and B additions, then examined their mechanical property evolution. Higher Mo concentrations in the $(\mathrm{Fe}_{60-x}\mathrm{Co}_{40}\mathrm{Mo}_x)_{99.6}\mathrm{B}_{0.3}\mathrm{C}_{0.1}$ alloys enhance both strength and ductility by enriching interfaces with Mo, thereby promoting the formation of interface complexes during annealing and enhancing mechanical properties (Supplementary Fig. 5). In the

$Fe_{49}Co_{40}Mo_{11}$ alloy, the absence of B/C segregation undermines ductility, limiting it to ~1% despite maintaining high strength (Supplementary Fig. 7). Together, these results highlight the pivotal role of interface complexes co-enriched with metallic and interstitial elements in enabling the simultaneous realization of ultrahigh strength and ductility.

Consistent with our conceptual design strategy, a defect-rich matrix capable of enduring severe rolling is essential for achieving ultrahigh strength. Experimental validation confirms the ST alloy's exceptional workability, withstanding over 85% thickness reduction during cold rolling and exhibiting compressive plasticity exceeding 80% (Supplementary Fig. 25). Its limited tensile ductility—fracturing at 2.76% strain—stems from coarse martensitic laths (Supplementary Fig. 26) where high-energy boundaries promote crack propagation, preventing activation of the transformation-induced plasticity effect under tension (Supplementary Fig. 13). Under rolling, the near-hydrostatic stress suppresses void opening and exceeds the critical stress for transformation-induced plasticity, thereby enhancing strain hardening and promoting progressive microstructural refinement into dislocation cells and SAGBs. This microstructural reorganization replaces brittle, high-energy lath interfaces with low-energy, defect-tolerant SAGBs, effectively decoupling the conventional strength–ductility trade-off. Consequently, the CR alloy achieves concurrent improvements in both yield strength and ductility, despite a substantial reduction in retained austenite.

To assess the universality of the interface complex strategy, we systematically investigated the mechanical properties and microstructural evolution of $(Fe_{50}Co_{40}(TiVMoW)_{10})_{99.6}B_{0.3}C_{0.1}$, $(Fe_{49}Co_{40}V_{10})_{99.6}B_{0.3}C_{0.1}$, $(Fe_{60}Co_{25}Ni_{10}Mo_{5})_{99.6}B_{0.3}C_{0.1}$ and $(Fe_{60}Co_{20}Ni_{15}Mo_{5})_{99.6}B_{0.3}C_{0.1}$ alloys, all processed via cold rolling followed by low-temperature annealing (Extended Data Figs. 3–6). The comparable strengthening responses observed in all alloys confirm the broad applicability of this interfacial engineering approach.

Conclusion

In summary, we demonstrate that simple cold rolling followed by low-temperature annealing enables the introduction of dislocations and interface complexes, driving a near-single-phase martensitic alloy to exceed a tensile yield strength of 3 GPa. During annealing, Mo, C and B cosegregate at high-density SAGBs, forming interface complexes that stabilize these boundaries and create effective pinning sites. These complexes obstruct dislocation motion and preserving dislocation transmission, striking a balance between strength and ductility. As a result, the alloy achieves a tensile yield strength of 3.05 GPa and a fracture elongation of 5.13%. This simple, broadly applicable strategy marks a promising advance in the design of next-generation ultrahigh-strength structural alloys.

Online content

Any methods, additional references, Nature Portfolio reporting summaries, source data, extended data, supplementary information, acknowledgements, peer review information; details of author contributions and competing interests; and statements of data and code availability are available at https://doi.org/10.1038/s41563-026-02479-9.

References

1. Jiang, S. H. et al. Strain hardening mediated by coherent nanoprecipitates in ultrahigh-strength steels. *Acta Mater.* **213**, 116984 (2021).
2. Wang, Y. et al. A low-alloy high-carbon martensite steel with 2.6GPa tensile strength and good ductility. *Acta Mater.* **158**, 247–256 (2018).
3. Li, Y. et al. Ductile 2-GPa steels with hierarchical substructure. *Science* **379**, 168–173 (2023).
4. Bain, E. C. The nature of martensite. *Trans. Am. Inst. Min. Metall. Pet. Eng.* **70**, 25 (1924).
5. Morsdorf, L., Tasan, C. C., Ponge, D. & Raabe, D. 3D structural and atomic-scale analysis of lath martensite: effect of the transformation sequence. *Acta Mater.* **95**, 366–377 (2015).
6. Morito, S., Yoshida, H., Maki, T. & Huang, X. Effect of block size on the strength of lath martensite in low carbon steels. *Mater. Sci. Eng. A* **438–440**, 237–240 (2006).
7. Shamsujjoha, M. Evolution of microstructures, dislocation density and arrangement during deformation of low carbon lath martensitic steels. *Mater. Sci. Eng. A* **776**, 139039 (2020).
8. Erlings, J. G. & Schapink, F. W. On thein situ relaxation of interphase interfaces. *J. Mater. Sci.* **15**, 381–386 (1980).
9. He, B. B. et al. High dislocation density-induced large ductility in deformed and partitioned steels. *Science* **357**, 1029–1032 (2017).
10. Liu, L. et al. Making ultrastrong steel tough by grain-boundary delamination. *Science* **368**, 1347–1352 (2020).
11. Li, Q. et al. 3 GPa dual-phase stainless steel from synergistic heterogeneous structure and nano-precipitate. *Mater. Res. Lett.* **13**, 207–216 (2024).
12. Niu, M. et al. Precipitate evolution and strengthening behavior during aging process in a 2.5 GPa grade maraging steel. *Acta Mater.* **179**, 296–307 (2019).
13. Guo, F. et al. Achieving good ductility in 2.1 GPa grade maraging steel. *Mater. Sci. Eng. A* **890**, 145886 (2024).
14. Pan, Q. et al. Atomic faulting induced exceptional cryogenic strain hardening in gradient cell-structured alloy. *Science* **382**, 185–190 (2023).
15. Hu, J. et al. Grain boundary stability governs hardening and softening in extremely fine nanograined metals. *Science* **355**, 1292–1296 (2017).
16. Zhang, J. et al. Unveiling the unique bifunctionality of $L1_2$-structured nanoprecipitates in a FeCoNiAlTi-type high-entropy alloy. *Adv. Powder Mater.* **2**, 100113 (2023).
17. Takeuchi, A. & Inoue, A. Classification of bulk metallic glasses by atomic size difference, heat of mixing and period of constituent elements and its application to characterization of the main alloying element. *Mater. Trans.* **46**, 2817–2829 (2005).
18. Li, Y. J., Ponge, D., Choi, P. & Raabe, D. Atomic scale investigation of non-equilibrium segregation of boron in a quenched Mo-free martensitic steel. *Ultramicroscopy* **159**, 240–247 (2015).
19. Zhou, Y. et al. Highly printable, strong, and ductile ordered intermetallic alloy. *Nat. Commun.* **16**, 1036 (2025).
20. Ivanisenko, Y. et al. Bulk nanocrystalline ferrite stabilized through grain boundary carbon segregation. *Adv. Eng. Mater.* **20**, 1800443 (2018).
21. Li, M., Peng, Z., Shang, Y. & Liu, Y. Phase equilibria in the Fe–Mo–Co system: experimental investigation and thermodynamic calculation. *Coatings* **13**, 1215 (2023).
22. Yeh, J. W., Chen, Y. L., Lin, S. J. & Chen, S. K. High-entropy alloys—a new era of exploitation. *Mater. Sci. Forum* **560**, 1–9 (2007).
23. Alberty, R. A. On the derivation of the Gibbs adsorption equation. *Langmuir* **11**, 3598–3600 (1995).
24. Gubicza, J. Annealing-induced hardening in ultrafine-grained and nanocrystalline materials. *Adv. Eng. Mater.* **22**, 1900507 (2019).
25. Morsdorf, L. et al. Carbon redistribution in quenched and tempered lath martensite. *Acta Mater.* **205**, 116521 (2021).
26. Schweizer, P. et al. Atomic scale volume and grain boundary diffusion elucidated by in situ STEM. *Nat. Commun.* **14**, 7601 (2023).
27. Li, Y. J., Ponge, D., Choi, P. & Raabe, D. Segregation of boron at prior austenite grain boundaries in a quenched martensitic steel studied by atom probe tomography. *Scr. Mater.* **96**, 13–16 (2015).
28. Wang, W., Zhang, S. & He, X. Diffusion of boron in alloys. *Acta Metall. Mater.* **43**, 1693–1699 (1995).

29. Schwaab, M. & Pinto, J. C. Optimum reference temperature for reparameterization of the Arrhenius equation. Part 1: problems involving one kinetic constant. *Chem. Eng. Sci.* **62**, 2750–2764 (2007).
30. Huang, Y. C., Lai, Y. C., Lin, Y. H. & Wu, S. K. A study on the severely cold-rolled and annealed quaternary equiatomic derivatives from quinary HfNbTaTiZr refractory high entropy alloy. *J. Alloys Compd.* **855**, 157404 (2021).
31. Xu, T. & Cheng, B. Kinetics of non-equilibrium grain-boundary segregation. *Prog. Mater. Sci.* **49**, 109–208 (2004).
32. Chamakura, J. N. et al. The quantitative relationship between non-linear stress–strain behaviour and dislocation structure in martensitic stainless steel. *Acta Mater.* **240**, 118364 (2022).
33. van Liempt, P. & Sietsma, J. A physically based yield criterion I. Determination of the yield stress based on analysis of pre-yield dislocation behaviour. *Mater. Sci. Eng. A* **662**, 80–87 (2016).
34. Hull, D. & Bacon, D. J. *Introduction to Dislocations* 4th edn (Butterworth-Heinemann, 2001).
35. Read, W. T. & Shockley, W. Dislocation models of crystal grain boundaries. *Phys. Rev.* **78**, 275–289 (1950).
36. Hughes, D. A. & Hansen, N. Microstructure and strength of nickel at large strains. *Acta Mater.* **48**, 2985–3004 (2000).
37. Chen, S. et al. Real-time observations of TRIP-induced ultrahigh strain hardening in a dual-phase CrMnFeCoNi high-entropy alloy. *Nat. Commun.* **11**, 826 (2020).
38. Couzinié, J. P. et al. On the room temperature deformation mechanisms of a TiZrHfNbTa refractory high-entropy alloy. *Mater. Sci. Eng. A* **645**, 255–263 (2015).
39. Caillard, D. & Martin, J. L. *Thermally Activated Mechanisms in Crystal Plasticity* 1st edn (Elsevier, 2003).
40. Wei, S. et al. On the plastic deformation of a CoCrFeNiW-C alloy at elevated temperatures: part I. Serrated plastic flow and its latent dynamics. *Acta Mater.* **242**, 118430 (2023).
41. Wei, X. et al. Achieving superior low-temperature toughness in high-strength low-carbon steel via controlling lath boundary segregation. *J. Mater. Res. Technol.* **24**, 1524–1536 (2023).
42. Seol, J. B. et al. Boron doped ultrastrong and ductile high-entropy alloys. *Acta Mater.* **151**, 366–376 (2018).
43. Yoo, J. et al. Effects of solid solution and grain-boundary segregation of Mo on hydrogen embrittlement in 32MnB5 hot-stamping steels. *Acta Mater.* **207**, 116661 (2021).
44. Geng, W. T., Freeman, A. J. & Olson, G. B. Influence of alloying additions on grain boundary cohesion of transition metals: first-principles determination and its phenomenological extension. *Phys. Rev. B* **63**, 165415 (2001).
45. Geng, W. T. & Freeman, A. J. Effect of Mo and Pd on the grain-boundary cohesion of Fe. *Phys. Rev. B* **62**, 6208–6214 (2000).
46. Guo, F. et al. Nanosized austenite and coherent nanoprecipitates making maraging steel strong and ductile. *Mater. Sci. Eng. A* **902**, 146605 (2024).
47. Zhai, Y. et al. Mechanical anisotropy of ultra strong-and-ductile lamellar dual-phase steel. *J. Mater. Res. Technol.* **28**, 3025–3036 (2024).
48. Lv, L., Fu, L., Sun, Y. & Shan, A. An investigation on the microstructure and mechanical properties in an ultrafine lamellar martensitic steel processed by heavy warm rolling and tempering. *Mater. Sci. Eng. A* **731**, 369–376 (2018).
49. Xu, T. et al. Effect of rolling temperature on the structural refinement and mechanical properties of dual-phase heterostructured low-carbon steel. *Metals* **12**, 115 (2022).
50. Caballero, F. G., Garcia-Mateo, C. & Miller, M. K. Design of novel bainitic steels: moving from ultrafine to nanoscale structures. *JOM* **66**, 747–755 (2014).
51. Chen, C.-Y. et al. Interaction between η-Ni_3Ti and reversed austenite within Custom 465 stainless steel: experimental evidence and related patents investigation. *Mater. Sci. Eng. A* **839**, 142852 (2022).
52. Zhu, F., Yin, Y. F. & Faulkner, R. G. Microstructural control of maraging steel C300. *Mater. Sci. Technol.* **27**, 395–405 (2011).
53. Chung, H. et al. Doubled strength and ductility via maraging effect and dynamic precipitate transformation in ultrastrong medium-entropy alloy. *Nat. Commun.* **14**, 145 (2023).
54. Niu, M. C. et al. Atomic-scale understanding of solute interaction effects on grain boundary segregation, precipitation, and fracture of ultrahigh-strength maraging steels. *Acta Mater.* **253**, 118972 (2023).
55. Jiang, W. et al. Effects of nanoprecipitates on mechanical properties in an ultra-high strength maraging stainless steel. *Mater. Charact.* **222**, 114837 (2025).
56. Niu, M. C. et al. Synergistic alloying effects on nanoscale precipitation and mechanical properties of ultrahigh-strength steels strengthened by Ni_3Ti, Mo-enriched, and Cr-rich co-precipitates. *Acta Mater.* **209**, 116788 (2021).
57. Li, Y. et al. A new 1.9 GPa maraging stainless steel strengthened by multiple precipitating species. *Mater. Des.* **82**, 56–63 (2015).
58. Jiang, S. et al. Ultrastrong steel via minimal lattice misfit and high-density nanoprecipitation. *Nature* **544**, 460–464 (2017).
59. Liu, Y. et al. Evolution of microstructures and mechanical properties with tempering temperature in a novel synergistic precipitation strengthening ultra-high strength steel. *Materials* **17**, 5314 (2024).
60. Wang, Z. H. et al. Designing ultrastrong maraging stainless steels with improved uniform plastic strain via controlled precipitation of coherent nanoparticles. *J. Mater. Sci. Technol.* **93**, 60–70 (2021).
61. Leitner, H., Schober, M., Schnitzer, R. & Zinner, S. Strengthening behavior of Fe–Cr–Ni–Al–(Ti) maraging steels. *Mater. Sci. Eng. A* **528**, 5264–5270 (2011).
62. Wang, S. et al. Dual nanoprecipitation and nanoscale chemical heterogeneity in a secondary hardening steel for ultrahigh strength and large uniform elongation. *J. Mater. Sci. Technol.* **185**, 245–258 (2024).
63. Wang, Y. et al. Effects of NiAl on precipitation behavior and mechanical properties of M2C strengthened secondary hardening steel. *J. Mater. Res. Technol.* **35**, 3107–3117 (2025).
64. Yang, B. et al. Achieving an extra-high-strength yet ductile steel by synergistic effects of TRIP and maraging. *Mater. Res. Lett.* **11**, 578–585 (2023).
65. Wang, L. J. et al. Ultrastrong steel strengthened by multiple shearable nanostructures. *J. Mater. Sci. Technol.* **161**, 245–257 (2023).
66. Kim, B. et al. The influence of silicon in tempered martensite: understanding the microstructure–properties relationship in 0.5–0.6wt.% C steels. *Acta Mater.* **68**, 169–178 (2014).
67. Junkui, L. et al. A medium-C martensite steel with 2.6 GPa tensile strength and large ductility. *Scr. Mater.* **228**, 115327 (2023).
68. Kim, Y.-K. et al. 2.47 GPa grade ultra-strong 15Co-12Ni secondary hardening steel with superior ductility and fracture toughness. *J. Mater. Sci. Technol.* **66**, 36–45 (2021).
69. Liu, Y. et al. Effects of prior austenite and primary carbides on mechanical properties of a novel 2.5 GPa grade ultra-high strength steel. *J. Iron Steel Res. Int.* **32**, 2064–2075 (2025).
70. Wang, J. et al. Enhanced mechanical properties of a high-carbon martensite steel processed by heavy warm rolling and tempering. *Mater. Sci. Eng. A* **872**, 144958 (2023).
71. Li, Y. et al. Achieving unprecedented yield strength of 2.2 GPa with high ductility in formed parts using strain-aging. *Scr. Mater.* **233**, 115521 (2023).

72. Liu, Z. et al. Enhanced strength-ductility synergy in a new 2.2 GPa grade ultra-high strength stainless steel with balanced fracture toughness: elucidating the role of duplex aging treatment. *J. Alloys Compd*. **928**, 167135 (2022).
73. Yuzbekova, D., Dudko, V., Kniaziuk, T. & Kaibyshev, R. Tempering behavior of an ultra-high-strength steel with 1.6 wt% Si at low to medium temperatures. *Mater. Sci. Eng. A* **896**, 146264 (2024).
74. Wu, B. et al. Constructing a heterogeneous microstructure in the CoCrFeNi-based high entropy alloy to obtain a superior strength-ductility synergy. *Mater. Sci. Eng. A* **886**, 145669 (2023).
75. Man, J. et al. The superior strength-ductility combination of a $(Ni_2FeCoCr)_{88.25}$-$Al_5Ti_3W_{1.5}Mo_{1.5}Nb_{0.75}$ high entropy alloy enhanced with the heterogeneous microstructure via thermo-mechanical processing. *Mater. Sci. Eng. A* **858**, 144137 (2022).
76. Zhou, S. et al. A remarkable toughening high-entropy-alloy wire with a bionic bamboo fiber heterogeneous structure. *Scr. Mater.* **226**, 115234 (2023).
77. Li, X. et al. Influence of Ti addition on the precipitation behavior and mechanical properties of Ni-7.9Cr-5.9W-22.2Mo superalloy. *J. Alloys Compd*. **946**, 169277 (2023).
78. Amar, A. et al. Ultra-strong and ductile medium entropy alloy with a dual heterogeneous microstructure. *Acta Mater.* **284**, 120645 (2024).
79. Liu, L., Zhang, Y. & Zhang, Z. Achieving ultrahigh strength and ductility via high-density nanoprecipitates triggering multiple deformation mechanisms in a dual-aging high-entropy alloy with precold deformation. *J. Mater. Sci. Technol.* **205**, 27–41 (2025).
80. Li, A. X. et al. Pursuing ultrahigh strength–ductility CoCrNi-based medium-entropy alloy by low-temperature pre-aging. *J. Mater. Sci. Technol.* **220**, 115–128 (2025).
81. Kwon, H. et al. High-density nanoprecipitates and phase reversion via maraging enable ultrastrong yet strain-hardenable medium-entropy alloy. *Acta Mater.* **248**, 118810 (2023).

Methods

Alloy design and fabrication

Fe, Co and Mo were selected as the principal elements for alloy design. The 1,350 °C isothermal section of the Fe–Co–Mo phase diagram[21] (Supplementary Fig. 1) was used to locate the single austenite region, a prerequisite for obtaining a fully martensitic matrix after quenching. An initial Mo content of 11 at.% lies at the boundary of this region and was therefore selected.

To refine the Fe/Co ratio, CALPHAD calculations (Thermo-Calc, TCFE13) were performed for the $Fe_xCo_{89-x}Mo_{11}$ system (Supplementary Fig. 2a). The results indicate a composition window of 39–59 at.% Fe for maintaining the desired phase stability. Within this window, we targeted the highest configurational entropy to enhance lattice distortion and defect density within the martensitic matrix, synthesizing four B- and C-bearing variants: $(Fe_{39}Co_{50}Mo_{11})_{99.6}B_{0.3}C_{0.1}$, $(Fe_{44}Co_{45}Mo_{11})_{99.6}B_{0.3}C_{0.1}$, $(Fe_{49}Co_{40}Mo_{11})_{99.6}B_{0.3}C_{0.1}$ and $(Fe_{54}Co_{35}Mo_{11})_{99.6}B_{0.3}C_{0.1}$. Room-temperature tensile tests on CR specimens showed comparable strength and ductility across all four alloys (Supplementary Fig. 2b). After annealing at 450 °C for 20 min, however, only the $(Fe_{44}Co_{45}Mo_{11})_{99.6}B_{0.3}C_{0.1}$ and $(Fe_{49}Co_{40}Mo_{11})_{99.6}B_{0.3}C_{0.1}$ alloys retained ductility, with the latter exhibiting the superior elongation. X-ray diffraction analysis and SEM analyses (Supplementary Fig. 2c–i) confirmed a martensitic matrix with minor boride particles in every case. On the basis of these findings, an Fe/Co ratio of 49/40 was adopted.

The Mo content was further optimized through CALPHAD calculations across the $Fe_{60-x}Co_{40}Mo_x$ system (Supplementary Fig. 3), followed by experimental validation with alloys containing 5, 7, 9, 11 and 13 at.% Mo. Alloys containing 5 and 13 at.% Mo exhibited poor workability due to the formation of brittle intermetallic phases (Supplementary Fig. 4). Within the processable window (7–11 at.% Mo), the strengthening contribution from interface complexes increased progressively with Mo content (Supplementary Fig. 5a). To determine the upper limit of Mo, a 12 at.% Mo alloy was examined (Supplementary Fig. 6). Although this alloy could be cold-rolled, its annealed counterpart showed extremely limited ductility (~1% elongation). Thus, 11 at.% Mo provides the optimum trade-off among phase stability, workability and segregation-induced strengthening, and the final composition $(Fe_{49}Co_{40}Mo_{11})_{99.6}B_{0.3}C_{0.1}$ was fixed for all subsequent studies.

Bulk ingots with the nominal composition of $(Fe_{49}Co_{40}Mo_{11})_{99.6}B_{0.3}C_{0.1}$ (at.%) were prepared by arc melting a mixture of high-purity raw materials (purity >99.95 wt.%) in a Ti-gettered, high-purity argon atmosphere. Each ingot was remelted at least eight times to ensure chemical homogeneity, then drop-cast into a water-cooled copper mould (dimensions $10 \times 10 \times 80$ mm^3). The as-cast sheets were homogenized at 1,200 °C for 2 h in an argon atmosphere, producing the ST alloy. These sheets were then cold-rolled to achieve a total thickness reduction of approximately 85%, resulting in the CR alloy. The ST specimen remained intact without visible cracks even after an 85% thickness reduction (Supplementary Fig. 25a), confirming its capacity for severe plastic deformation. Complementary uniaxial compression tests further reveal that the ST alloy can sustain compressive strains exceeding 80% (Supplementary Fig. 25b). These results underscore the fundamental difference between tensile and compressive stress states, explaining why limited tensile ductility does not hinder successful cold rolling. The 85% reduction ratio was selected as the optimal prestraining because insufficient reductions fail to accumulate the stored energy required for substantial interface complex formation, whereas higher reductions (for example, 92%) cause noticeable rolling cracks and reduce post-anneal ductility to ~2% (Supplementary Figs. 27 and 28). Finally, the CR alloy was annealed at 450 °C for 20 min and water-quenched to yield the CRA alloy. The 450 °C/20 min condition was identified as optimal annealing for interface complex strengthening through additional experimental verification (Supplementary Fig. 29). Annealing at ≥500 °C embrittled the alloy (Supplementary Fig. 29a), while extending the duration to 60 min increased strength at the expense of ductility (Supplementary Fig. 29b). Thus, annealing at 450 °C for 20 min achieves near saturation of interface complex strengthening while preserving the optimum strength–ductility balance. Moreover, although the processing window is well defined, superior mechanical properties are consistently reproduced (Supplementary Figs. 27–29), confirming that the proposed processing strategy possesses both reliable tolerance and broad applicability.

Mechanical properties testing

Room-temperature uniaxial tensile tests were conducted using a Shimadzu AGS-X-50 kN universal testing machine equipped with a Shimadzu non-contact digital video extensometer at an initial strain rate of 1.0×10^{-3} s^{-1}. Flat dog-bone specimens, with a gauge length of 20 mm and a cross-sectional area of 3.0×1.5 mm^2, were prepared along the longitudinal direction via electrical discharge machining. A minimum of three samples were tested for each condition to ensure statistical reliability.

Stress-relaxation tensile testing

Stress-relaxation tests were conducted to assess whether the observed high flow stress arises from variations in the governing thermally activated processes. Dog-bone-shaped tensile specimens with dimensions of $10 \times 2 \times 1.5$ mm^3 were prepared. The specimens were strained to 1.8% at a strain rate of 10^{-3} s^{-1}, after which the cross-head of the testing machine was halted and held at 1.8% strain for 400 s. During this holding period, the load was continuously recorded as a function of time. Each alloy underwent three independent stress-relaxation tests. The theoretical foundation of stress-relaxation testing lies in the stress-dependent Gibbs free energy ($\Delta G(\sigma)$), which quantifies the energy required for mobile dislocations to overcome metallurgical obstacles, such as interstitial clouds, short-range ordered domains, forest dislocations and precipitates. A key physical parameter derived from this analysis, the apparent activation volume ($V^{\text{app.}}$), represents the material volume involved in thermally activated processes under external stress. $V^{\text{app.}}$ is influenced by both the stress dependence of the mobile dislocation density and their velocity. It can be determined by fitting the stress-relaxation data to the following equation[39]:

$$\Delta\sigma(t) = -\frac{Nk_BT}{V^{\text{app.}}}\ln\left(1+\frac{t}{c_r}\right). \qquad (1)$$

Here, $\Delta\sigma(t)$ represents the true stress drop as a function of time (t). k_B, T, $V^{\text{app.}}$ and C_r denote the Boltzmann constant, absolute temperature, apparent activation volume and time constant, respectively. The factor N, which converts the applied normal stress (σ) to resolved shear stress (τ), was set to 3.06, consistent with the uniaxial tensile loading condition of the specimens[82].

Microstructure characterization

Synchrotron radiation ex situ HEXRD experiments were performed at the Beijing Synchrotron Radiation Facility using a high-energy monochromatic X-ray beam (60.05 keV, wavelength 0.02065 nm). A CeO_2 standard was utilized to calibrate the detector position and orientation. Two-dimensional (2D) diffraction patterns were recorded using a Pilatus3X 2M detector, The 2D images were subsequently integrated into one-dimensional (1D) HEXRD patterns along the azimuthal angle from 0° to 20° via the Dioptas software. In situ synchrotron HEXRD experiments were conducted at the Powder Diffraction and Total Scattering Beamline P02.1 of PETRA III at Deutsches Elektronen-Synchrotron (DESY) in Hamburg, Germany[83,84]. The beamline operated at 60 keV, delivering a monochromatic X-ray with a wavelength of ~0.020738 nm. Tensile measurements were carried out using a Kammrath & Weiss stress rig, capable of withstanding loads up to 5 kN, positioned between the incident beam and the 2D detector. The subsized tensile specimens measured 12 mm in length, 2 mm in width and approximately 0.6 mm in thickness. Tensile tests were conducted at room temperature with a constant cross-head speed, and the initial strain rate was approximately ~1×10^{-3} s^{-1}. The sample-to-detector distance was about 1 m, with the incident beam size measuring 0.6 mm × 0.6 mm. A LaB_6 standard was used for calibration to determine the detector distance and instrument broadening. During tensile testing, 2D diffraction patterns were captured every 5 s using the Varex XRpad 4343CT fast area detector (2,880 pixels × 2,880 pixels). The resulting 2D Debye–Scherrer diffraction images were then integrated into 1D diffraction profiles using GSAS-II software[85]. SEM was conducted on Tescan Mira 3 LMU FEG operated at 20 kV. Electron backscattered diffraction (EBSD) analysis was carried out on a Zeiss Sigma 300 microscope equipped with an Oxford Symmetry detector operating at 15 kV. TEM imaging was performed using a FEI Talos F200X at 200 kV. Aberration-corrected scanning TEM measurements and EDS mapping were performed on a Thermo Fisher Scientific Themis Z microscope operated at 300 kV with a ChemiSTEM EDS system. SEM samples were prepared through mechanical polishing with diamond plaster followed by vibratory polishing with colloidal silica suspension (Vibra 304). EBSD samples underwent additional electropolishing in a solution of 10% perchloric acid and 90% ethanol (vol.%) at −20 °C after mechanical polishing. TEM samples were prepared via twin-jet electropolishing in a 10% perchloric acid and 90% ethanol (vol.%) solution at −20 °C following mechanical grinding.

APT analysis

APT analysis was performed on the CR and CRA alloys using a Cameca Leap 5000 XR system, operating at a pulse repetition rate of 125 kHz, a pulse fraction of 20% and a test temperature of 60 K. Data reconstruction and analysis were performed using the Cameca AP Suite 6.0 software. Error bars for the 1D compositional profile were calculated using

$$2\sigma = \sqrt{\frac{c_{\mathrm{i}}(1 - c_{\mathrm{i}})}{N}}, \tag{2}$$

where N represents the total number of atoms in the analysed volume, and c_{i} is the composition of each solute.

Data availability

Source data are provided with this paper. Other data generated or analysed during this study are included in the Supplementary Information.

References

82. Wei, S. & Tasan, C. C. On the plastic deformation of a CoCrFeNiW-C alloy at elevated temperatures: part II. Grain boundary sliding and damage mechanisms. *Acta Mater.* **252**, 118898 (2023).
83. Dippel, A.-C. et al. Beamline P02.1 at PETRA III for high-resolution and high-energy powder diffraction. *J. Synchrotron Rad.* **22**, 675–687 (2015).
84. Ma, Y. et al. Phase boundary segregation-induced strengthening and discontinuous yielding in ultrafine-grained duplex medium-Mn steels. *Acta Mater.* **200**, 389–403 (2020).
85. Shen, J. et al. Evolution of microstructure and deformation mechanisms in a metastable $Fe_{42}Mn_{28}Co_{10}Cr_{15}Si_5$ high entropy alloy: a combined in-situ synchrotron X-ray diffraction and EBSD analysis. *Mater. Des.* **238**, 112662 (2024).

Acknowledgements

This research was funded by the National Natural Science Foundation of China (grant nos. 52371153, 52471174 and 12522203), the Fundamental Research Funds for the Central Universities (grant nos. 531118010621 and 531118010671) and the National Natural Science Foundation of Hunan Province (grant no. 2025JJ30017). We acknowledge DESY (Hamburg, Germany), a member of the Helmholtz Association HGF, for the provision of experimental facilities. Parts of this research were carried out at PETRA III beamline P02.1, and we thank A. S. J. Méndez for her assistance. Beamtime was allocated for proposals I-20230050 and I-20230183.

Author contributions

Y.S., Z. Lei and Z. Lu supervised and conceived of this project. R.L. and M.J. carried out the materials fabrication as well as the mechanical and microstructure characterizations. J.L. and S. Wang conducted the discrete dislocation dynamics simulation and analysed the data. X.C. conducted the APT characterizations and analysed the data. X.Z. performed the density functional theory and MC simulation and analysed the data. C.M. conducted the TEM experiments. R.L., S.D., Y.M., S. Wei, A.S., F.Z. and C.P. conducted the synchrotron X-ray diffraction experiments and analysed the data. R.L., Y.S., Z. Lei and Z. Lu wrote and revised the paper. All authors discussed the results and commented on the paper.

Competing interests

The authors declare no competing interests.

Additional information

Extended data is available for this paper at https://doi.org/10.1038/s41563-026-02479-9.

Supplementary information The online version contains supplementary material available at https://doi.org/10.1038/s41563-026-02479-9.

Correspondence and requests for materials should be addressed to Yunzhu Shi, Zhifeng Lei or Zhaoping Lu.

Peer review information *Nature Materials* thanks Jae-il Jang and Eun Soo Park for their contribution to the peer review of this work.

Reprints and permissions information is available at www.nature.com/reprints.

https://doi.org/10.1038/s41563-026-02479-9

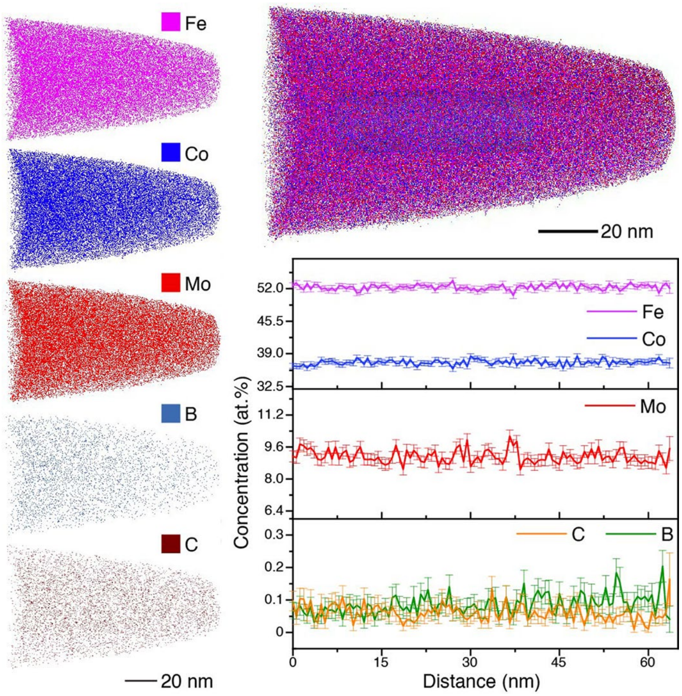

Extended Data Fig. 1 | Atom probe tomography measurements of the CR alloy. The experimental dataset demonstrates the uniform distribution of all elements in the CR alloy. The error bars are standard deviations of the mean.

https://doi.org/10.1038/s41563-026-02479-9

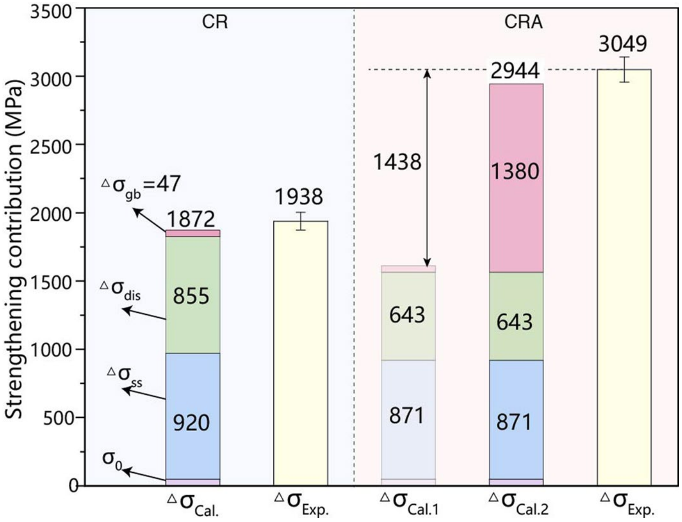

Extended Data Fig. 2 | Calculation of the yield strength. Comparison of the calculated strength contributions $\Delta\sigma_{\mathrm{Cal}}$ and experimental strength contributions $\Delta\sigma_{\mathrm{Exp}}$ for the CR and CRA alloys. The calculation results agree well with the experimental values. σ_0, $\Delta\sigma_{\mathrm{ss}}$, $\Delta\sigma_{\mathrm{dis}}$, and $\Delta\sigma_{\mathrm{gb}}$ represent the lattice friction strengthening, solid-solution hardening, dislocation strengthening, and grain boundary strengthening, respectively. The data points and error bars represent the mean ± standard deviation (s.d.) taken from four independently tensile samples.

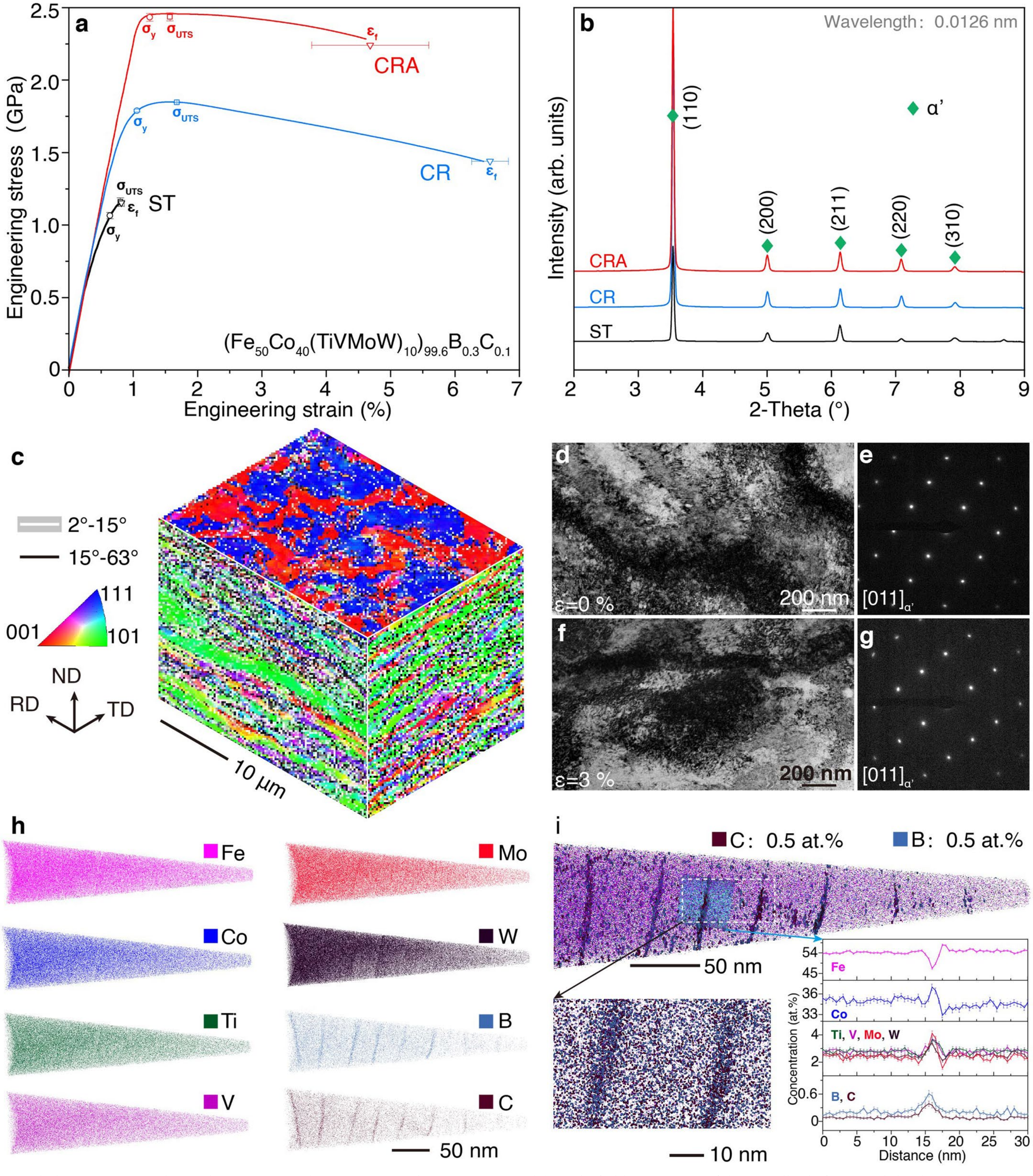

Extended Data Fig. 3 | Mechanical properties and microstructural characterization of the (Fe50Co40(TiVMoW)10)99.6B0.3C0.1 alloy. **a**, Room-temperature engineering stress–strain curves showing progressive strengthening from the ST (1.065 GPa) and CR (1.778 GPa) states to the CRA state, which exhibits a yield strength of 2.433 GPa and a fracture elongation of ~5%. The data points and error bars represent the mean ± standard deviation (s.d.) taken from three independently tensile samples. **b**, HEXRD patterns indicating that all processing states are predominantly martensitic. **c**, Three-dimensional EBSD orientation maps of the CRA alloy revealing retained deformation textures: <101> along RD–ND and ND–TD planes, and <001 > / < 111> in the RD–TD plane. **d**, **f**, Bright-field TEM images of the CRA alloy before tensile loading and at 3% strain, respectively, showing a high density of dislocations in the TD–RD plane. **e**, **g**, Corresponding SAED patterns confirming a single martensitic phase. **h**, Atom probe tomography (APT) measurements of the CRA alloy. **i**, Three-dimensional APT reconstruction with 0.5 at.% iso-composition surfaces for C and B, illustrating the co-segregation of Co, Ti, V, Mo, W, B, and C at SAGBs, indicative of interface complexes formation. The one-dimensional compositional profile (blue cylinders) compares the chemical composition across the SAGB and the matrix, and the enlarged view (white square) details the C and B distributions across the SAGB. The error bars are standard deviations of the mean.

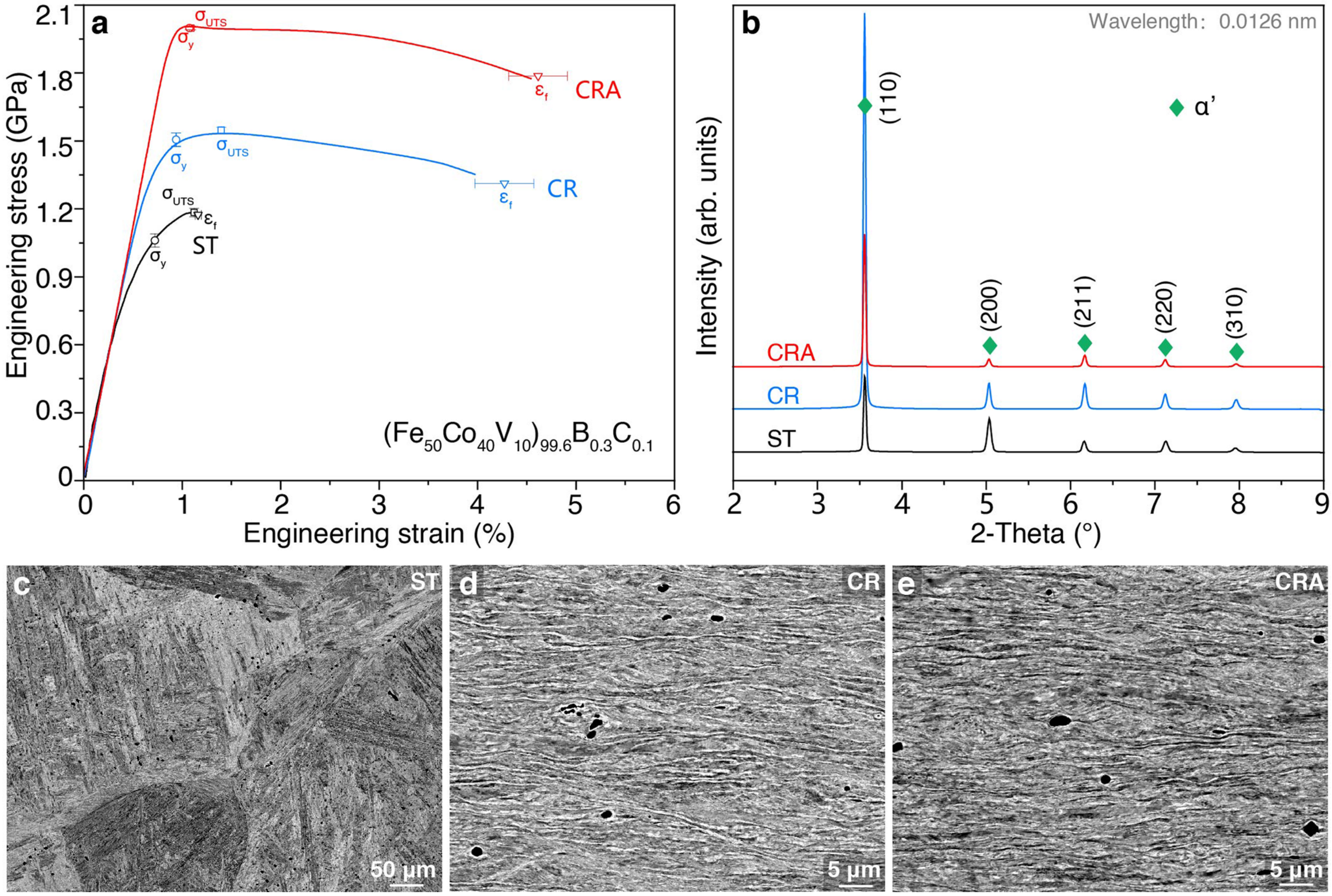

Extended Data Fig. 4 | Mechanical properties and microstructural characterization of the (Fe50Co40V10)99.6B0.3C0.1 alloy. a, Room-temperature engineering stress–strain curves showing enhanced tensile yield strength from 1.061 GPa (ST) and 1.506 GPa (CR) to 1.998 GPa in the CRA state, while retaining ~5% fracture elongation. The data points and error bars represent the mean ± standard deviation (s.d.) taken from three independently tensile samples. **b**, HEXRD patterns indicating that all processing states (ST, CR, CRA) predominantly consist of the martensite phase. **c**-**e**, SEM images of the ST, CR, and CRA alloys, respectively, showing typical lath martensite morphology with minor boride phases. The formation of V–B–C interface complexes contributes to the crucial strengthening effect observed in the CRA alloy.

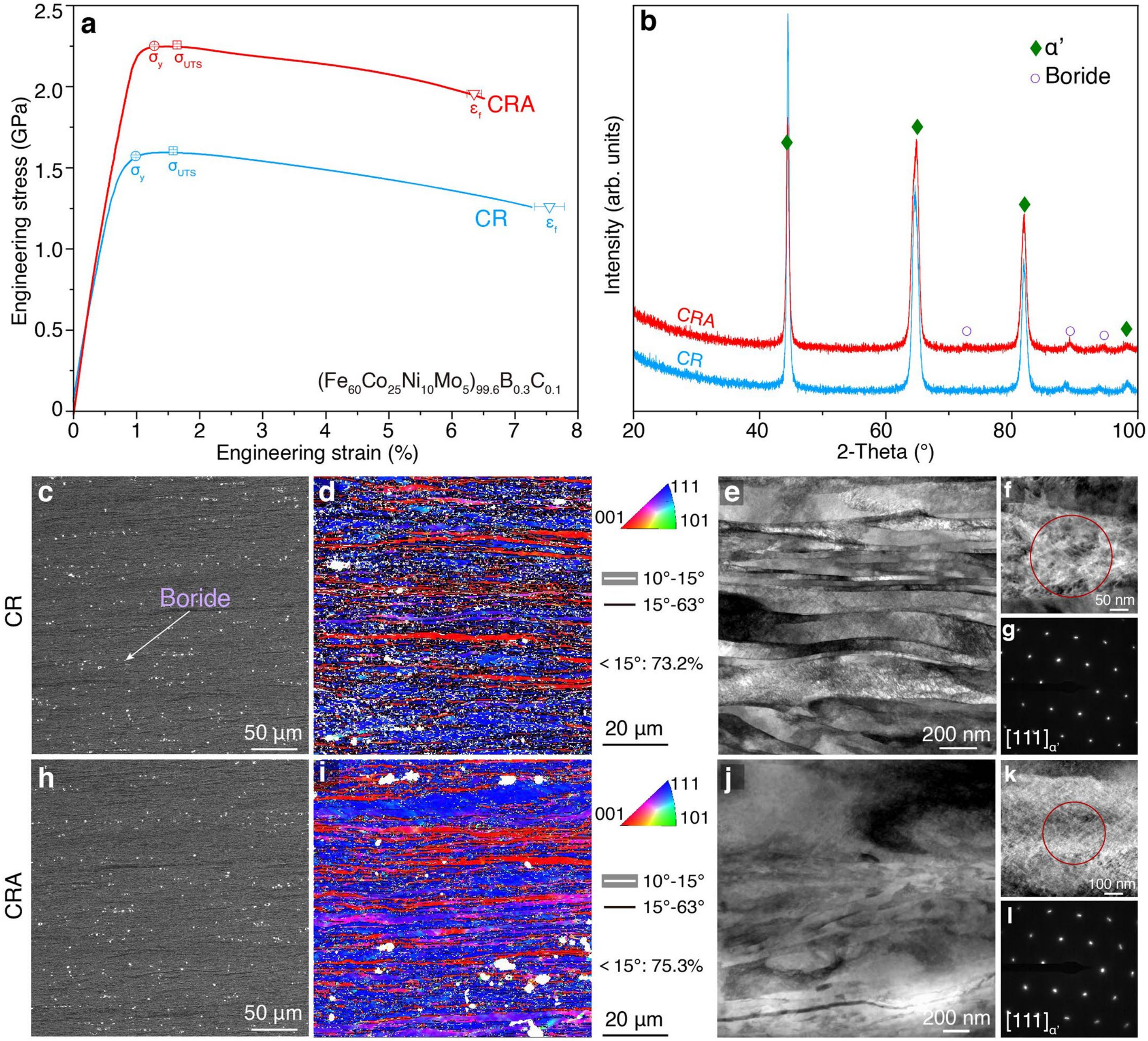

Extended Data Fig. 5 | Mechanical properties and microstructural characterization of the (Fe60Co25Ni10Mo5)99.6B0.3C0.1 alloy. **a**, Room-temperature engineering stress–strain curves showing an increase in tensile yield strength from 1.57 GPa in the cold-rolled (CR) state to 2.25 GPa after annealing (CRA) without sacrificing ~7% fracture elongation. The data points and error bars represent the mean ± standard deviation (s.d.) taken from three independently tensile samples. **b**, XRD patterns confirming predominant bcc martensite in both CR and CRA states. **c, h**, SEM and **d, i**, EBSD images of the CR and CRA alloys, respectively, revealing typical lath martensite morphology with minor boride phases. **e, j**, Bright-field transmission electron microscopy (BF-TEM) images of the CR and CRA alloys, respectively. **f, k**, Corresponding dark-field TEM (DF-TEM) images, and **g, l**, SAED patterns acquired from the regions marked by red circles in **f** and **k**, respectively.

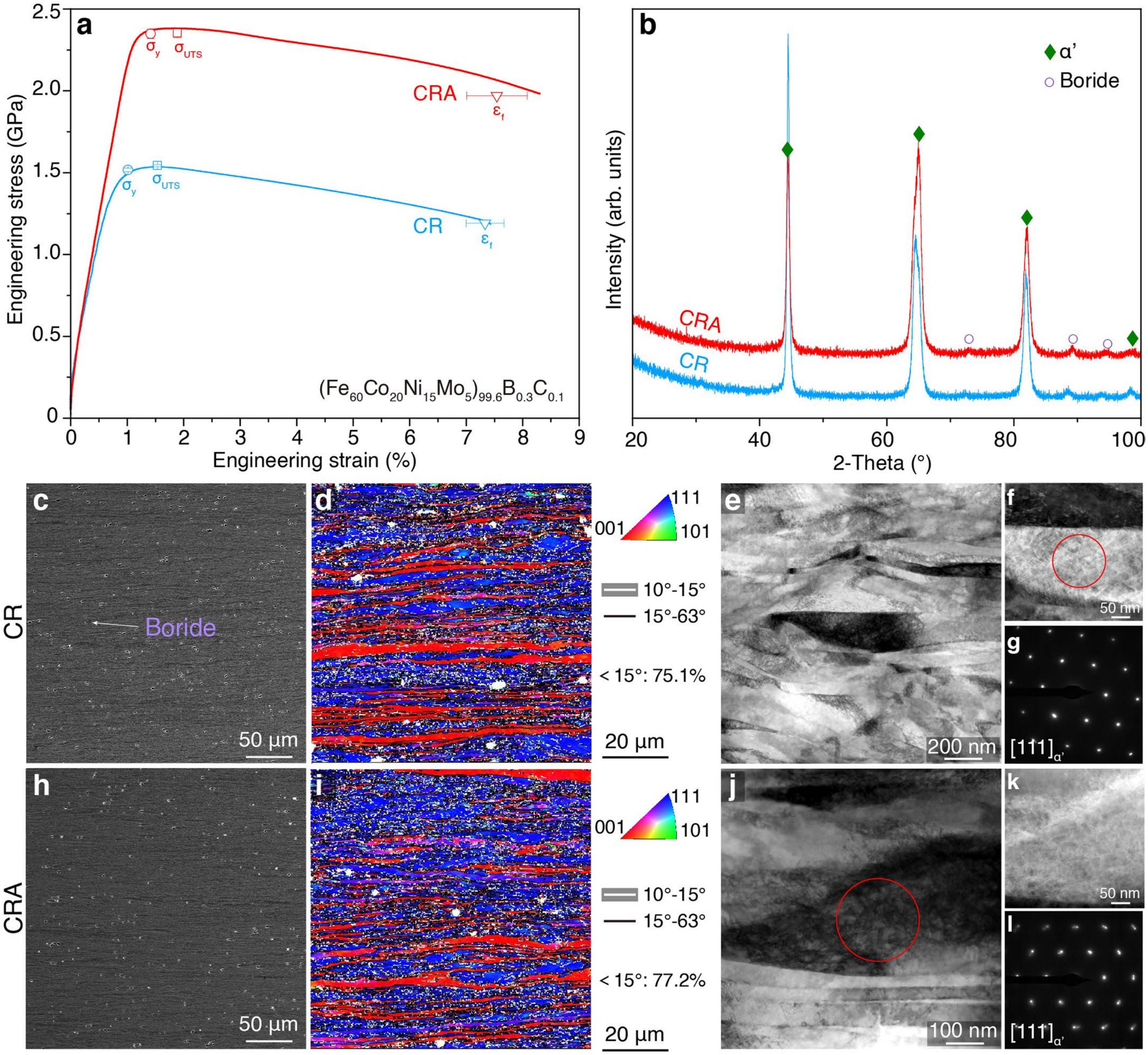

Extended Data Fig. 6 | Mechanical properties and microstructural characterization of the (Fe60Co20Ni15Mo5)99.6B0.3C0.1 alloy. **a**, Room-temperature engineering stress–strain curves showing an increase in tensile yield strength from 1.52 GPa in the cold-rolled (CR) state to 2.35 GPa after annealing (CRA), while maintaining ~8% fracture elongation. The data points and error bars represent the mean ± standard deviation (s.d.) taken from three independently tensile samples. **b**, XRD patterns confirming that both CR and CRA states are predominantly martensitic. **c, h**, SEM and **d, i**, EBSD images of the CR and CRA alloys, respectively, revealing typical lath martensite morphology with minor boride phases. **e, j**, BF-TEM images, **f, k**, corresponding DF-TEM images, and **g, l**, SAED patterns acquired from the regions marked by red circles in **f** and **j**, respectively, for the CR and CRA alloys.